

Hippocampal Spine Head Sizes Are Highly Precise

Thomas M Bartol^{1*}, Cailey Bromer¹, Justin Kinney^{1,2}, Michael A. Chirillo³, Jennifer N. Bourne³, Kristen M. Harris^{3*}, Terrence J Sejnowski^{1,4*}

¹Howard Hughes Medical Institute, the Salk Institute for Biological Studies, La Jolla, CA 92037

²McGovern Institute for Brain Research, Massachusetts Institute of Technology, Cambridge, MA, 02139

³Center for Learning and Memory, Department of Neuroscience, University of Texas, Austin, TX 78712-0805, USA

⁴Division of Biological Sciences, University of California at San Diego, La Jolla, CA 92093

*Correspondence to. E-mail: bartol@salk.edu, kmh2249@gmail.com, terry@salk.edu

J. Kinney - Current address: MIT

J. Bourne - current address: Univ. Colorado, Denver

Hippocampal synaptic activity is probabilistic and because synaptic plasticity depends on its history, the amount of information that can be stored at a synapse is limited. The strong correlation between the size and efficacy of a synapse allowed us to estimate the precision of synaptic plasticity. In an electron microscopic reconstruction of hippocampal neuropil we found single axons making two or more synaptic contacts onto the same dendrites which would have shared histories of presynaptic and postsynaptic activity. The postsynaptic spine heads, but not the spine necks, of these pairs were nearly identical in size. The precision is much greater than previous estimates and requires postsynaptic averaging over a time window many seconds to minutes in duration depending on the rate of input spikes and probability of release.

One Sentence Summary:

Spine heads on the same dendrite that receive input from the same axon are the same size.

Excitatory synapses on dendritic spines of hippocampal pyramidal neurons have a wide range of sizes that are highly correlated with their synapse sizes and strengths¹⁻⁷. Due to high failure rate and other sources of stochastic variability, these synapses transmit unreliably individual presynaptic action potentials. Nonetheless, the sizes and strengths of these synapses can increase or decrease according to the relative timing of presynaptic inputs and postsynaptic spikes⁸. Prior work suggests that pairs of spines on the same dendrite contacting the same axon are more similar in size than those from the same axon on different dendrites⁹. Here we evaluated this axon-spine coupling in three-dimensional reconstructions from serial electron microscopy reconstruction (3DEM) of hippocampal neuropil from 3 adult rats, to determine this similarity with higher precision and the time window over which pre- and post-synaptic histories would need to be coordinated.

In a $6 \times 6 \times 5 \mu\text{m}^3$ complete 3DEM from the middle of stratum radiatum in hippocampal area CA1^{10,11}, we identified 149 dendritic branches, 446 axons, and 449 synapses. We measured spine head volume and surface area, surface area of the postsynaptic density (PSD) adjacent to the presynaptic active zone, and quantified the number of vesicles at the 288 spines fully contained within the volume. Strong correlations between these metrics are consistent with previous observations^{1,4} and confirm the typicality of our sample (Figs. 1, 2, S1). To reduce error, we averaged over multiple independent spine volume measurements for each spine (Fig. 1A, Fig. S2). We determined that the relationship between PSD area and spine head volume did not differ significantly across different dendritic branches (Fig. S3). The correlation between spine head area and spine head volume accounted for 99% of the variance, despite the wide range in spine head shapes and dimensions (Fig. S1E), which suggests that the accuracy of our measurements matched the precision of the spine. We also measured spine neck volume and found no significant correlation between the neck and PSD area (Fig. 1C) or spine head volume (Fig. 1D).

Next, we analyzed spine volumes according to their axonal connectivity and dendritic origin. Pairs of spines on the same dendrite that received input from the same axon (“axon-coupled”), were of the same size and had nearly identical head volumes (Fig. 3, S4-S6). We compared this sample of 10 axon-coupled pairs to those identified from the two additional animals, for a total of 17 pairs. When plotted against one another, the paired head volumes were highly correlated with slope 0.91, and despite the small sample size, were highly significantly different from random pairings of spines (Fig. 3C, S7A, KS, $p = 0.0002$). Similarly, there was a strong positive correlation between their paired PSD areas (Fig. 3D) and number of presynaptic docked vesicles (Fig. 3E). These features of axon-coupled spines from the same dendrite spanned the distribution of the overall spine population (Fig. S1). In contrast, the spine neck volumes of the pairs were not well-correlated (Fig. 3F), indicating a different function.

The outliers in this set of pairs (Fig. 3C, gray points “k, l, m”) are from comparison of three spines on a single dendritic branch receiving synaptic input from a common multi-synaptic bouton. A larger central spine between two similar in size (Fig. 3B, “k, l, m”) produces one same size pair (“k”) and two different size pairs (“l”, “m”). This unusual configuration is probably driven by processes that differ from the other pairs^{9,12}. Excluding this triple synapse, the median

value of the coefficient of variation of volume differences between pairs was $CV = 0.083$ and was constant across the range of spine sizes (Fig. S8).

This near-identical size relationship does not hold for axon-coupled spines on different dendritic branches (Fig. 4B, $CV = 0.39$, $n = 128$, example Fig. 4A), nor for non-axon-coupled spines on the same or different dendrites (Figs. 4E, 4F, example Fig. 4D), all cases that would have different activation histories. The volumes of axon-coupled different-dendrite spines are no different from the volumes of random pairs when plotted against one another (KS, $p = 0.89$, Figs. 4B, 4C, S7A) and the distribution of their sizes was no different from the whole population (KS, $p = 0.44$). The number of docked vesicles for pairs on different dendrites (Fig. S9B) is not different from random pairings (KS, $p = 0.15$). The sizes of pairs of axon-coupled spines on the same or different dendritic branches is unaffected by separation distance (Fig. S10), proximity of glia processes to the synapses (Fig. S11)^{13,14}, or location of mitochondria in the axon¹⁵.

Spine heads ranged in size over a factor of 60 from smallest to largest, which allows ~24 different strengths to be reliably distinguished across this range, assuming $CV = 0.083$ and a 75% discrimination threshold (Fig. S12). This corresponds to 4.6 bits of information that can be stored at each synapse (see Methods). The precision of the majority of smaller spines is as good as that of the minority larger spines (Fig. S8), suggesting that accurately maintaining the size of every synapse, regardless of size and strength, could be important for the function, flexibility and computational power of the hippocampus.

How can the high precision in spine head volume be achieved despite the many sources of stochastic variability observed in synaptic responses? These include: 1) The low probability of release from the presynaptic axon in response to an action potential⁵; 2) Stochastic fluctuations in the opening of postsynaptic NMDA receptors, with only a few of the 2-20 conducting at any time¹⁶; 3) Location of release site relative to AMPA receptors¹⁷⁻¹⁹ 4) Few voltage-dependent calcium channels (VDCCs) in spines that affect synaptic plasticity (smallest spines contain none)^{20,21}; 5) VDCCs depress after back propagating action potentials²²; 6) Capacity for local ribosomal protein synthesis in some spines while others depend on transport of proteins from the dendrites^{23,24}; 7) Homeostatic mechanisms for synaptic scaling may vary^{25,26}; 8) Presence or absence of glia^{13,27}; and 9) Frequency of axonal firing²⁸.

To explain the high precision observed in spine head volumes, we propose that time-window averaging smooths out fluctuations due to plasticity and other sources of variability. To set a lower bound on averaging time we chose to examine neurotransmitter release probability as a single source of variability. Release can be analyzed using a binomial model in which n presynaptic action potentials, each with a probability p_r of releasing one or more vesicles, leads to a mean number of releases $\mu = n*p_r$ having variance $\sigma^2 = n*p_r*(1-p_r)$. The coefficient of variation around the mean is $CV = \sqrt{\sigma^2}/\mu = \sqrt{[(1-p_r)/(n*p_r)]}$ and can be compared with the measured values. Therefore, the number of spikes that are needed to reduce the variability to achieve a given CV is $n = (1-p_r)/(p_r*CV^2)$. Table 1 gives averaging time windows $T = n/R$, where R is spiking rate of the presynaptic axon, for representative values of p_r and a range of spiking rates. Accounting for other known sources of variability at dendritic spines would require even longer time windows.

Phosphorylation of calcium/calmodulin-dependent protein kinase II (CaMKII), required for spike-timing dependent plasticity processes, integrates calcium signals over minutes to hours and is a critical step in enzyme cascades leading to structural changes induced by long-term potentiation (LTP) and long-term depression (LTD)²⁹, including rearrangements of the cytoskeleton³⁰. The time course over which CaMKII integrates calcium signals is within the range of time windows we predict would be needed for averaging (Table 1). Similar time windows occur in synaptic tagging and capture: Inputs that are too weak to trigger LTP or LTD can be “rescued” by a stronger input to neighboring synapses if it occurs within an hour^{31,32}, which also requires CaMKII^{33,34}.

Due to the many sources of variability, information encoded at a single synapse cannot be read out with a single input spike. Read out of the information over multiple spikes might reflect a sampling strategy designed for energetic efficiency since it is the physical substrate that must be stable for long-term memory retention, not the read out of individual spikes³⁵.

Previous lower bounds on the precision of synaptic strength in the hippocampus were based on whole spine volume^{9,36}. Our estimate based on spine head volume is an order of magnitude greater precision. Complementing our observations and analysis, highly correlated p_r at multiple contacts between the axon of a given layer 2/3 pyramidal neuron and the same target cell has been reported³⁷. Thus, our findings suggest that 3DEM measurements of neocortical dendritic spines may reveal similarly precise estimates of synaptic efficacy.

Fig. 1. Spine head volumes, but not neck volumes, are correlated with PSD areas. A) Example segmentation of spine head (yellow), neck (gray), and PSD area (red). B) Strong correlation between PSD area and spine head volume. No correlation between spine neck volume and C) PSD area or D) spine head volume. Regression lines in red and error bars for each data point represent SEM based on multiple tracers who also edited each spine. Equations are based on the log-log distributions, with r^2 values indicated, and $n=288$ complete spines.

Fig. 2. Presynaptic docked vesicle numbers are correlated with PSD areas and spine head volumes, but not with spine neck volumes. A) All 31,377 presynaptic vesicles. B) *En face* view of the 24 docked vesicles (gray spheres) viewed through an axon (green) onto the PSD (red) of example spine (yellow). C) Number of docked vesicles is correlated with PSD area and D) spine head volume, but not correlated with E) spine neck volume. Regression lines, SEM, and r^2 are as in Fig. 1, $n = 237$ complete axonal boutons, each associated with one of the 288 complete spines. One tracer marked vesicles, hence no SEM.

Fig. 3. Spine head volumes and PSD areas, but not neck volumes, are highly correlated between pairs of axon-coupled same-dendrite spines. A) Visualization of a pair of spines (gray necks) from the same dendrite (yellow) with synapses (red, indicated by white arrows) on the same axon (black stippling) with presynaptic vesicles (white spheres). B) All axon-coupled same-dendrite spine pairs (colors as in 1A, pair c is elaborated in 3A). Strong correlations with slopes near 1 (dashed diagonal line) occur between paired C) spine head volumes ($slope=0.91$), D) PSD areas ($slope=0.74$), and E) docked vesicles ($slope=0.91$); but not F) spine neck volumes ($slope=0.49$). Larger values from each pairing are plotted on the X axis. Regression lines (red) include the 10 a-j pairings (blue points) and 7 pairs from 2 additional animals (red points in C), but do not include triplet bouton pairings (k-m, gray points).

Fig. 4. Paired spine head volumes are not correlated when they are not both axon and dendrite coupled. A) Representative visualization and B) plot showing lack of correlation between spine head volumes of all pairs of axon-coupled spines on different dendrites ($n=128$). C) Similarly, randomly associated pairs of spine head volumes were not correlated. D) Representative visualization and plots show lack of correlation between spine head volumes from randomly selected pairs ($n=128$) of non-axon-coupled spines E) on the same or F) different dendrites. Color scheme and regression analyses as in Fig. 3.

Supplementary Materials:

Materials and Methods

Figures S1-S12

References and Notes

1. Harris, K. M. & Stevens, J. K. Dendritic spines of CA1 pyramidal cells in the rat hippocampus: serial electron microscopy with reference to their biophysical characteristics. *J. Neurosci.* **9**, 2982–2997 (1989).
2. Lisman, J. & Harris, K. Who's been nibbling on my PSD: is it LTD? *J. Physiol. Paris* **88**, 193–195 (1994).
3. Harris, K. M. & Sultan, P. Variation in the number, location and size of synaptic vesicles provides an anatomical basis for the nonuniform probability of release at hippocampal CA1 synapses. *Neuropharmacology* **34**, 1387–1395 (1995).
4. Schikorski, T. & Stevens, C. F. Quantitative ultrastructural analysis of hippocampal excitatory synapses. *J. Neurosci.* **17**, 5858–5867 (1997).
5. Murthy, V. N., Schikorski, T., Stevens, C. F. & Zhu, Y. Inactivity Produces Increases in Neurotransmitter Release and Synapse Size. *Neuron* **32**, 673–682 (2001).
6. Branco, T., Staras, K., Darcy, K. J. & Goda, Y. Local dendritic activity sets release probability at hippocampal synapses. *Neuron* **59**, 475–485 (2008).
7. Bourne, J. N., Chirillo, M. A. & Harris, K. M. Presynaptic ultrastructural plasticity along CA3→CA1 axons during long-term potentiation in mature hippocampus. *J. Comp. Neurol.* **521**, 3898–3912 (2013).
8. Bi, G. Q. & Poo, M. M. Synaptic modifications in cultured hippocampal neurons: dependence on spike timing, synaptic strength, and postsynaptic cell type. *J. Neurosci.* **18**, 10464–10472 (1998).
9. Sorra, K. E. & Harris, K. M. Occurrence and three-dimensional structure of multiple synapses between individual radiatum axons and their target pyramidal cells in hippocampal area CA1. *J. Neurosci.* **13**, 3736–3748 (1993).
10. Mishchenko, Y. *et al.* Ultrastructural analysis of hippocampal neuropil from the connectomics perspective. *Neuron* **67**, 1009–1020 (2010).
11. Kinney, J. P. *et al.* Extracellular sheets and tunnels modulate glutamate diffusion in hippocampal neuropil. *J. Comp. Neurol.* **521**, 448–464 (2013).
12. Sorra, K. E., Fiala, J. C. & Harris, K. M. Critical assessment of the involvement of perforations, spinules, and spine branching in hippocampal synapse formation. *J. Comp. Neurol.* **398**, 225–240 (1998).
13. Ventura, R. & Harris, K. M. Three-dimensional relationships between hippocampal synapses and astrocytes. *Journal of Neuroscience* **19**, 6897–6906 (1999).
14. Witcher, M. R., Kirov, S. A. & Harris, K. M. Plasticity of perisynaptic astroglia during synaptogenesis in the mature rat hippocampus. *Glia* **55**, 13–23 (2007).

15. Billups, B. & Forsythe, I. D. Presynaptic mitochondrial calcium sequestration influences transmission at mammalian central synapses. *Journal of Neuroscience* **22**, 5840–5847 (2002).
16. Nimchinsky, E. A., Yasuda, R., Oertner, T. G. & Svoboda, K. The number of glutamate receptors opened by synaptic stimulation in single hippocampal spines. *Journal of Neuroscience* **24**, 2054–2064 (2004).
17. Franks, K. M., Stevens, C. F. & Sejnowski, T. J. Independent sources of quantal variability at single glutamatergic synapses. *Journal of Neuroscience* **23**, 3186–3195 (2003).
18. Ashby, M. C., Maier, S. R., Nishimune, A. & Henley, J. M. Lateral diffusion drives constitutive exchange of AMPA receptors at dendritic spines and is regulated by spine morphology. *Journal of Neuroscience* **26**, 7046–7055 (2006).
19. Kusters, R., Kapitein, L. C., Hoogenraad, C. C. & Storm, C. Shape-induced asymmetric diffusion in dendritic spines allows efficient synaptic AMPA receptor trapping. *Biophys. J.* **105**, 2743–2750 (2013).
20. Mills, L. R. *et al.* N-type Ca²⁺ channels are located on somata, dendrites, and a subpopulation of dendritic spines on live hippocampal pyramidal neurons. *J. Neurosci.* **14**, 6815–6824 (1994).
21. Magee, J. C. & Johnston, D. Characterization of single voltage-gated Na⁺ and Ca²⁺ channels in apical dendrites of rat CA1 pyramidal neurons. *The Journal of Physiology* **487** (Pt 1), 67–90 (1995).
22. Yasuda, R., Sabatini, B. L. & Svoboda, K. Plasticity of calcium channels in dendritic spines. *Nat Neurosci* **6**, 948–955 (2003).
23. Ostroff, L. E., Fiala, J. C., Allwardt, B. & Harris, K. M. Polyribosomes redistribute from dendritic shafts into spines with enlarged synapses during LTP in developing rat hippocampal slices. *Neuron* **35**, 535–545 (2002).
24. Sutton, M. A. & Schuman, E. M. Dendritic protein synthesis, synaptic plasticity, and memory. *Cell* **127**, 49–58 (2006).
25. Turrigiano, G. G. The self-tuning neuron: synaptic scaling of excitatory synapses. *Cell* **135**, 422–435 (2008).
26. Bourne, J. N. & Harris, K. M. Coordination of size and number of excitatory and inhibitory synapses results in a balanced structural plasticity along mature hippocampal CA1 dendrites during LTP. *Hippocampus* **21**, 354–373 (2011).
27. Clarke, L. E. & Barres, B. A. Emerging roles of astrocytes in neural circuit development. *Nat. Rev. Neurosci.* **14**, 311–321 (2013).
28. Callaway, J. C. & Ross, W. N. Frequency-dependent propagation of sodium action potentials in dendrites of hippocampal CA1 pyramidal neurons. *J. Neurophysiol.* **74**, 1395–1403 (1995).

29. Kennedy, M. B., Beale, H. C., Carlisle, H. J. & Washburn, L. R. Integration of biochemical signalling in spines. *Nat. Rev. Neurosci.* **6**, 423–434 (2005).
30. Kramár, E. A. *et al.* Synaptic evidence for the efficacy of spaced learning. *Proc Natl Acad Sci USA* **109**, 5121–5126 (2012).
31. Frey, U. & Morris, R. G. M. Synaptic tagging and long-term potentiation. *Nature* **385**, 533–536 (1997).
32. O'Donnell, C. & Sejnowski, T. J. Selective memory generalization by spatial patterning of protein synthesis. *Neuron* **82**, 398–412 (2014).
33. Redondo, R. L. & Morris, R. G. M. Making memories last: the synaptic tagging and capture hypothesis. *Nat. Rev. Neurosci.* **12**, 17–30 (2011).
34. de Carvalho Myskiw, J., Furini, C. R. G., Benetti, F. & Izquierdo, I. Hippocampal molecular mechanisms involved in the enhancement of fear extinction caused by exposure to novelty. *Proc Natl Acad Sci USA* **111**, 4572–4577 (2014).
35. Laughlin, S. B. & Sejnowski, T. J. Communication in neuronal networks. *Science* **301**, 1870–1874 (2003).
36. O'Connor, D. H., Wittenberg, G. M. & Wang, S. S.-H. Graded bidirectional synaptic plasticity is composed of switch-like unitary events. *Proc. Natl. Acad. Sci. U.S.A.* **102**, 9679–9684 (2005).
37. Koester, H. J. & Johnston, D. Target cell-dependent normalization of transmitter release at neocortical synapses. *Science* **308**, 863–866 (2005).
38. Edwards, J. *et al.* VolRoverN: Enhancing Surface and Volumetric Reconstruction for Realistic Dynamical Simulation of Cellular and Subcellular Function. *Neuroinformatics* **12**, 277–289 (2014).

Acknowledgements

We are grateful to Dr. Mary Kennedy, Dr. Charles Stevens, Dr. Cian O'Donnell, and Dr. Krishnan Padmanabhan, for discussions on many aspects of synaptic spines and CaMKII, Josef Spacek, and Dylan Yokoyama for data acquisition, and Libby Perry and Robert Smith for serial sectioning and image acquisition. This research was supported by NIH grants NS44306 (to Mary Kennedy), NS21184, MH095980, and NS074644 (to Kristen Harris), P41-GM103712, MH079076 and the Howard Hughes Medical Institute (to T. Sejnowski).

Table 1. Lower bounds on time window for averaging binomially distributed synaptic input to achieve CV=0.083.

Release probability (p_r)	Presynaptic spikes (n)	Averaging time (R = 1 Hz)	Averaging time (R = 25 Hz)
0.1	1306	21.8 min	52.2 sec
0.2	581	9.68 min	23.2 sec
0.5	145	2.42 min	5.8 sec

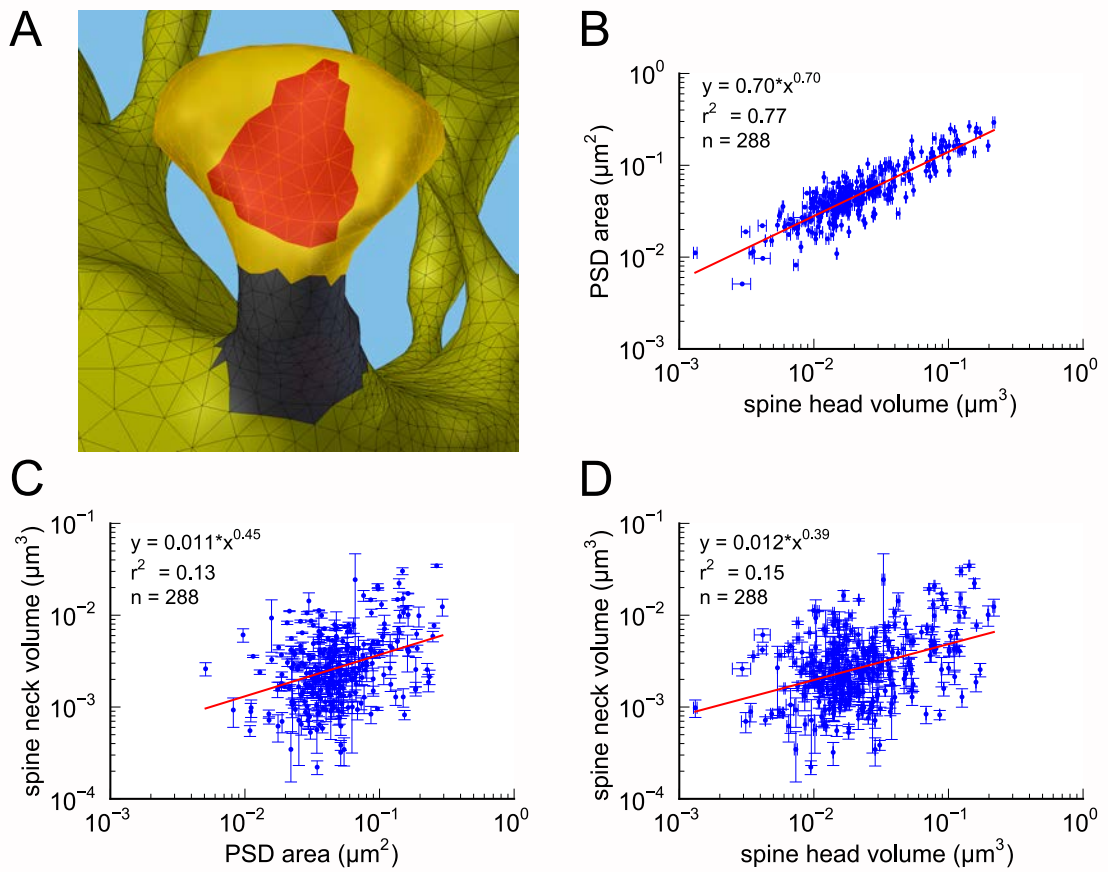


Figure 1

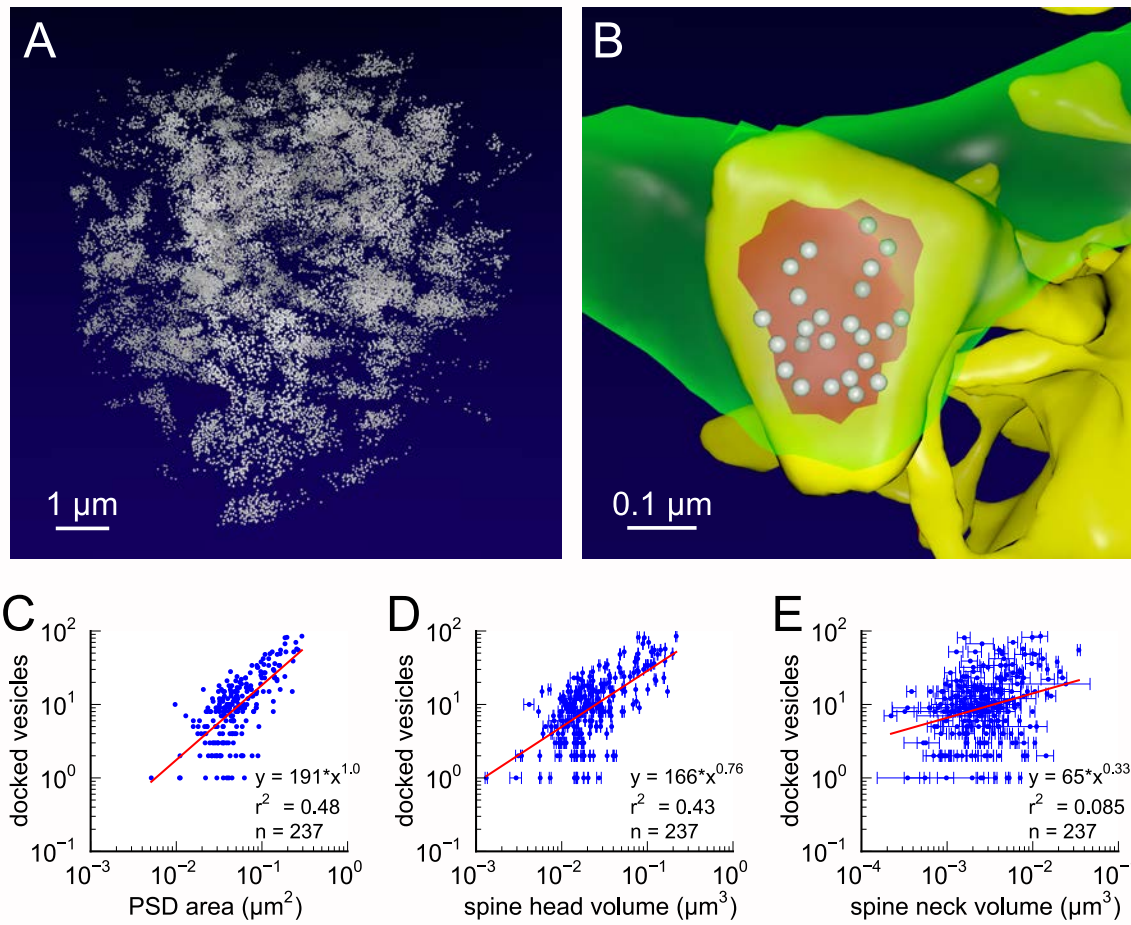


Figure 2

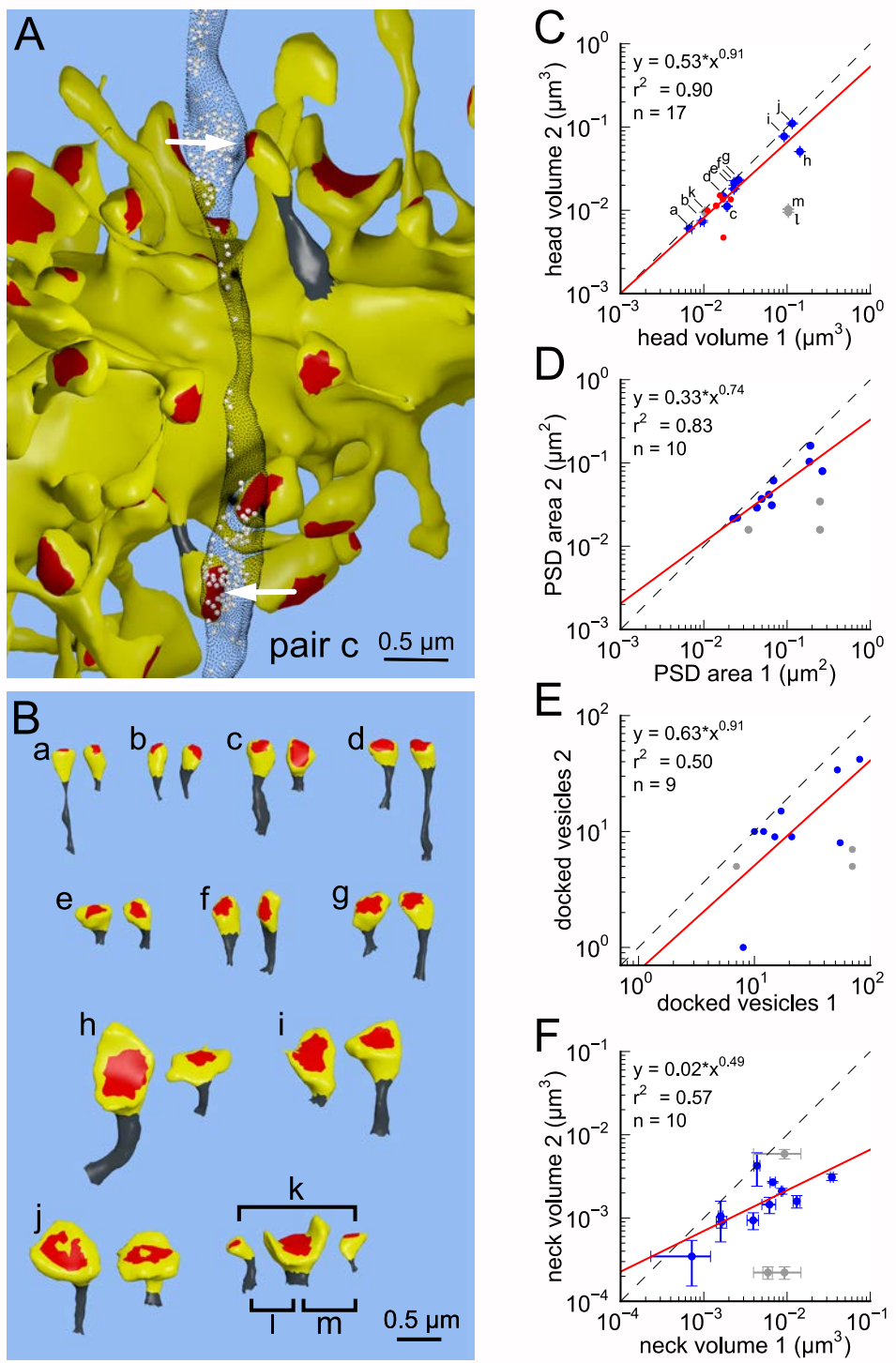


Figure 3

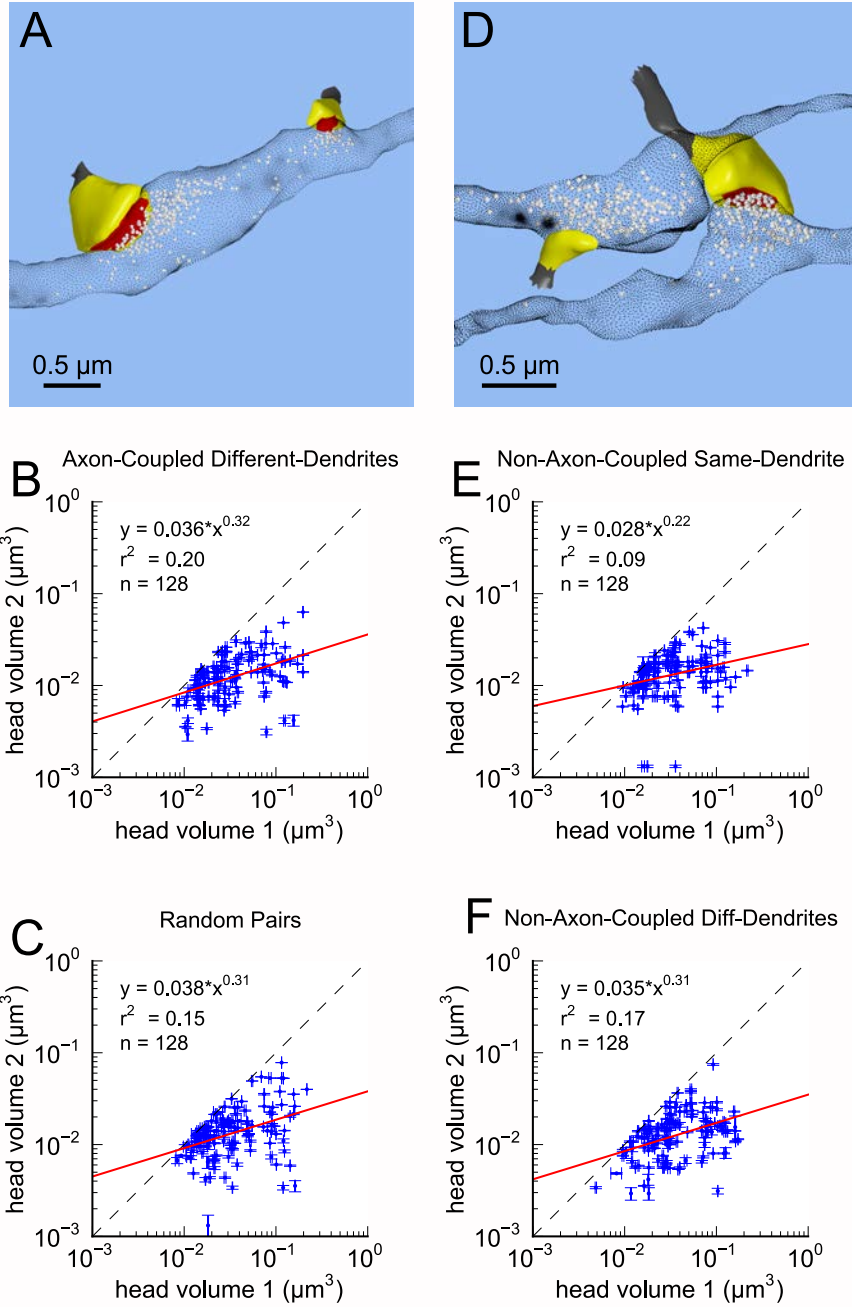


Figure 4

Supplementary Materials

Materials and Methods

Reconstruction of Neuropil

Images were obtained from serial thin sections in the middle of stratum radiatum of hippocampal area CA1 from three adult male rats (55-65 days old)^{7,10}. One set of images was used to make a dense model of 6 x 6 x 5 μm^3 of hippocampal neuropil and processed as previously described¹¹. To perform an accurate and robust geometric analysis of the dendrites, dendritic spines, axons, and glial processes in the dense reconstruction, it was necessary to correct the reconstructed surface meshes for artifacts and make them into computational-quality meshes as described elsewhere^{11,38}. The other two sets of images were part of a prior study⁷ in which subsets of dendrites and axons had been reconstructed and here we identified 7 additional axon-coupled synaptic pairs on 4 dendrites thereby increasing to 17 the number of axon-coupled dendrite-coupled spine pairs. Similarly high-quality surface meshes were created from this subset of spines, which served also to confirm consistency in the main finding across animals (Fig. 3C).

The postsynaptic densities (PSDs) and presynaptic active zones (AZs) were identified in the ssTEM images by their electron density and presence of closely apposed presynaptic vesicles. We devised a method to segment the postsynaptic density-active zone (PSD-AZ) features in the electron micrographs and mark their pre- and post-synaptic locations as subregions of the membrane in the final 3D mesh. To accomplish this, contours were hand-drawn on each serial section micrograph closely encompassing, as a single closed contour, the pre- and post-synaptic extent of the electron dense region. Taken together, the stack of contours for a given PSD-AZ forms a 3D capsule which encloses the entire feature. VolRoverN³⁸ was used to reconstruct the 3D surface of the capsule enclosing each PSD-AZ pair in 3D. Because these capsules enclose the intracellular domain of both the PSD and AZ they also overlap with the pre- and post-synaptic membrane associated with these subcellular features. Each of these closed capsules was then used as a “3D lasso” to tag mesh triangles of the pre- and post-synaptic membrane contained within the lasso, marking the enclosed membrane area as a synaptic contact region -- PSD on the postsynaptic dendrite and AZ on the presynaptic axon. Figure 1A shows a postsynaptic contact area labeled in red on a dendritic spine.

The reconstructed neuropil models were then visualized and analyzed using Blender, a free, open-source tool for 3D computer graphics modeling (<http://blender.org>). A total of 449 synaptic contacts were found in the dense reconstructed volume of neuropil. We excluded a number of synapses from the analysis if they were partially clipped by the edge of the dataset (141), or were shaft synapses (20) leaving 288 valid synapses on dendritic spines in the dense model. An additional 70 spines were excluded from the analysis of axon-coupled spines as the axon which contacted these spines did not contact any other spines within the reconstructed volume. Example visualizations of the spines and axons, generated using Blender, are shown in Figs. 1A, 2A, 2B, 3A, 3B, 4A, 4D, S4, and S5.

Segmentation of Dendritic Spines

Blender's functionality is user-extensible via a Python interface for creating add-ons. We created a Python add-on for Blender that enabled the selection of the mesh triangles of the dendrite corresponding to the spine head and whole spine of each individual spine. Our add-on tagged each selected set of triangles with metadata for the spine name and geometric attributes of the head, whole spine, and neck as described below.

The selection of the spine head was made by hand based on a standardized procedure in which the junction between the head and neck was visually identified as half-way along the concave arc as the head narrows to form the neck (see Fig. 1A). To select the whole spine, a similar visual judgment was made to locate the junction where the neck widens as it joins the dendritic shaft.

Once the appropriate area was selected, the tool was designed to automatically create the convex hull of the selected region. The closed mesh formed by the Boolean intersection of the convex hull and the dendritic branch was used to determine the measured volume of the spine head or whole spine. The volume of the neck was calculated by taking the difference between these two measurements.

Areas were computed from the selected regions for spine head and whole spine. Active zone and postsynaptic density areas were calculated using regions that had been determined during the hand-drawn reconstruction phase described above.

Distances between spine heads along the axon were calculated as the Euclidean distance between the centroids of the PSD/AZ regions. Distances between whole spines along the dendritic shaft were calculated as the Euclidean distance between the spine necks to shaft junctions. Glial classification, mitochondria classification and shape classification were performed by hand using set criteria.

Estimation of Measurement Error of Spine Head Volume

Some error in the measurement of spine head volume is expected to occur in the human judgment required to segment the dendritic spines into whole spine, head, and neck. To estimate this error, the valid spines in the dense model were segmented and measured a total of four times per spine (twice each by two people). The standard error of the mean in spine head volume decreases with volume and is less than 5% for the majority of spines with a median error of about 1% (Fig. S2). The head volumes in the two partially reconstructed datasets were only measured once.

Segmentation of Synaptic Vesicles and Estimation of Docked Vesicles

Synaptic vesicles in the presynaptic terminals, totaling 31377 in number, were identified along with their 3D locations within the dense reconstruction. Of the 449 presynaptic terminals, we excluded 192 terminals from the analysis due to truncation at the edge of the volume, and 20 terminals at shaft synapses, leaving 237 valid terminals. A visualization of all the synaptic vesicles in the reconstruction is shown in Fig. 2A.

Positive identification of docked vesicles in these ssTEM datasets is problematic due to the thickness of the sections and density of the staining. To estimate docked vesicles, we counted the number of vesicles whose centers were located within 100 nm of the presynaptic membrane across from the postsynaptic density of a given spine. Of the 31377 vesicles, 3437 were labeled as docked according to this criterion which yielded estimates in good agreement with previous estimates^{3,4}(Figs. 2B-D). An *en face* view of the docked vesicles at one synapse is shown in Fig. 2B.

Statistical Analysis

All statistical analysis and plots were generated using Python 2.7 (<http://python.org>) with NumPy, SciPy, and Matplotlib. The distributions of spine head volume, spine head area, spine neck volume, PSD area, and AZ area were highly skewed with a long tail at larger values (Fig. 1). Consequently, all regression analysis was performed using Pearson's linear regression on the data after applying a log-normal transformation (r^2 values shown in Figs. 1-4, Figs. S1-S3, S6-S10).

The coefficient of variation (CV) of the population of spine pairings (Figs. 3 and 4) was calculated as the median value of the CVs of each individual pair. The CV of each individual pair is simply the standard deviation of the volumes of the pair divided by the mean volume of the pair (Fig. S8).

Population distributions were highly skewed making it necessary to make comparisons of distributions using non-parametric methods. We used the two-sample Kolmogorov-Smirnov (KS) test to make these comparisons in Figs. 3 and 4.

Estimation of number of distinguishable spine sizes and bits of precision in spine size

To estimate the number of distinguishable spine sizes and corresponding bits of precision we calculated the number of distinct Gaussian distributions of spine sizes, each with a certain mean size and standard deviation that together would cover the entire range of spine head sizes seen in Fig. S1A. Fig. S8 demonstrates that it is reasonable to assume that the CV of each sub-distribution is a constant value of 0.083. From this CV, the mean of each sub-distribution can be chosen to achieve a total of 25% overlap with adjacent distributions giving a 75% discrimination threshold.

The 75% confidence interval, z , of a Gaussian distribution is given by:

$$z = \text{sqrt}(2)*\text{erf}^{-1}(0.75)$$

The spacing, s , of adjacent intervals of mean, μ , is given by:

$$s = \mu * 2 * CV * z$$

The number, N , of such distributions that would span the factor of 60 range of spine sizes is:

$$N = \log(60)/\log(1 + 2 * CV * z)$$

$$N = 23.42$$

The number of bits of precision implied by N distinguishable distributions is given by:

$$bits = \log_2(N)$$

$$bits = 4.55$$

Fig. S12 shows that ~24 distinguishable distributions can cover the entire range of spine sizes, implying that there are ~4.6 bits of precision in the spine size.

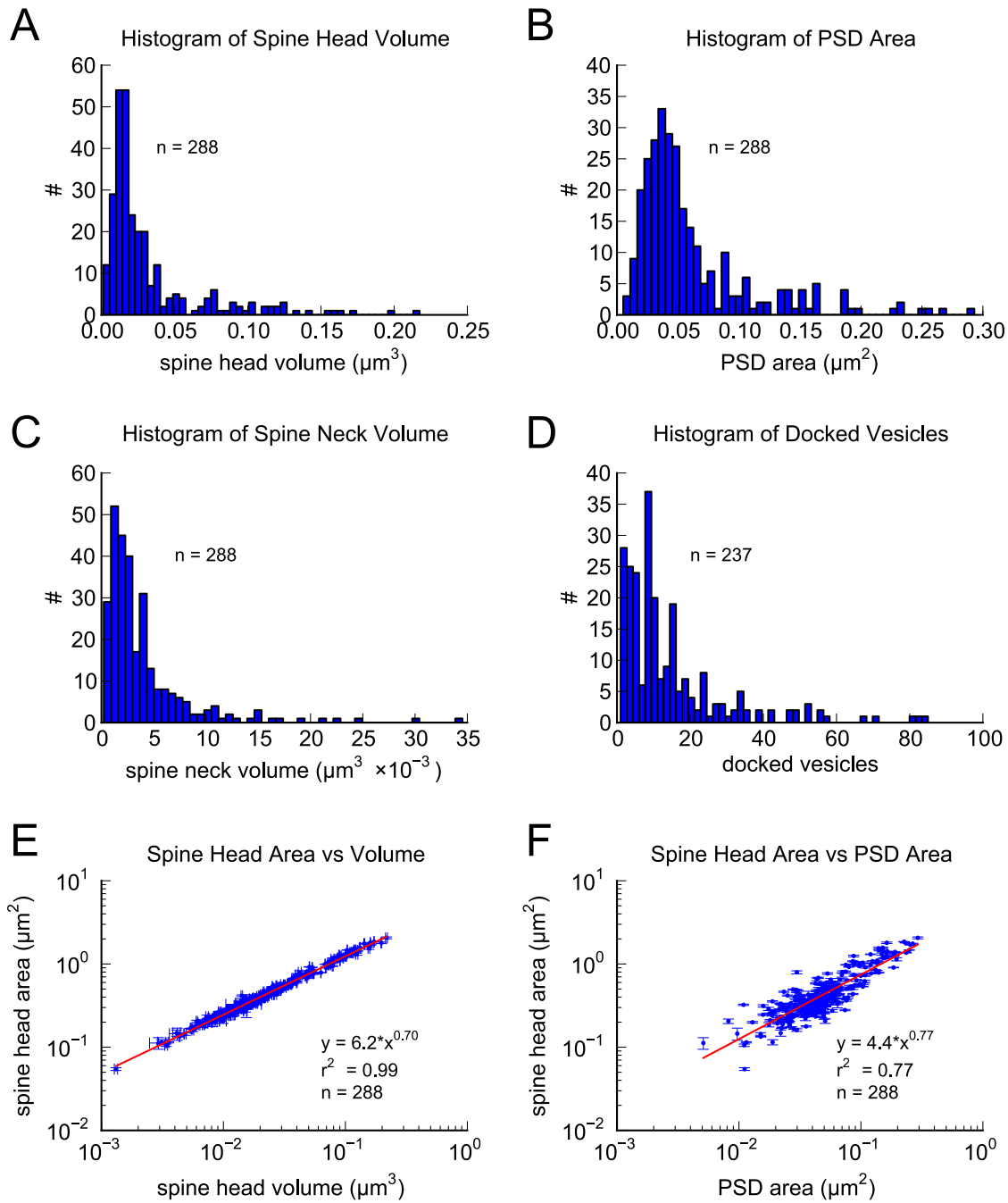


Figure S1

Fig. S1. Morphometric analysis of 288 complete spines in reconstruction. Distributions of A) spine head volumes, B) PSD areas, C) spine neck volumes, and D) docked vesicles are highly skewed with a long tail. Spine head area is highly correlated with E) spine head volume and F) PSD area. Regression lines in red and error bars for each data point represent SEM based on multiple tracers who edited each spine. PSD areas, and vesicles were traced only once. Equations are based on regression of log-log distributions, with r^2 values indicated.

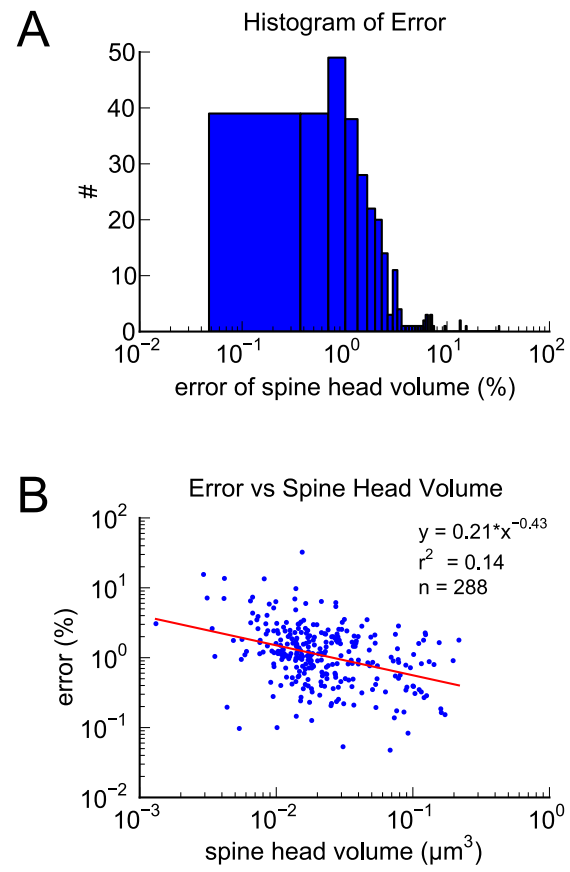


Figure S2

Fig. S2. Estimation of Measurement Error. A) Histogram of the measurement error across all spines measured. B) Measurement error plotted against spine head volume.

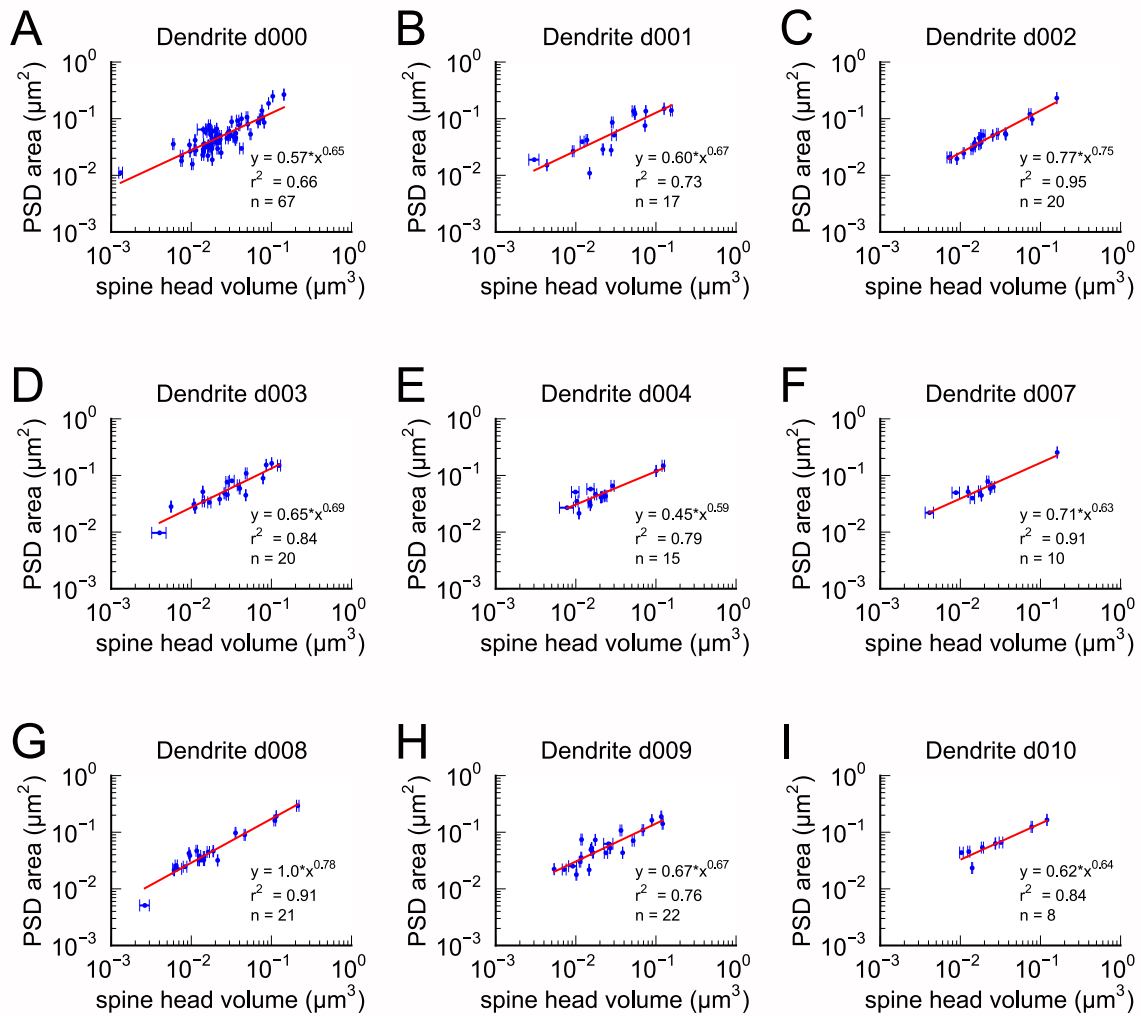


Figure S3

Fig. S3. Area of postsynaptic density plotted against spine head volume. Nine individual dendritic branches all have similar slopes that are not significantly different showing the uniformity of this comparison across dendrites.

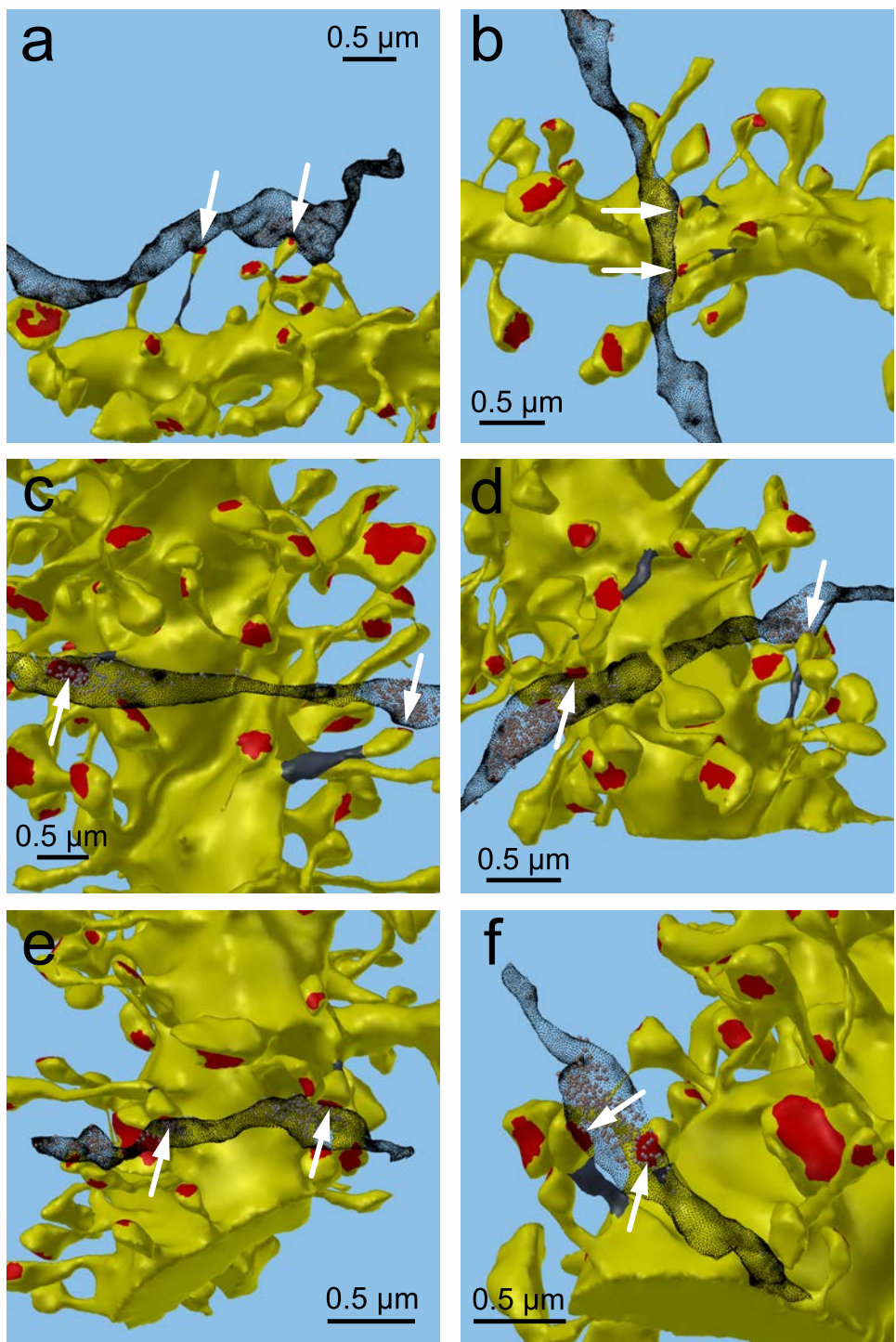


Figure S4

Fig. S4. Axon-coupled same dendrite pairs a-f. Large white arrows indicate the red PSDs of the spine pairs, the edited necks are dark gray, and the axons are stippled black with vesicles inside. These illustrate how the axon weaves through the neuropil, synapses with two spines yet passes by others.

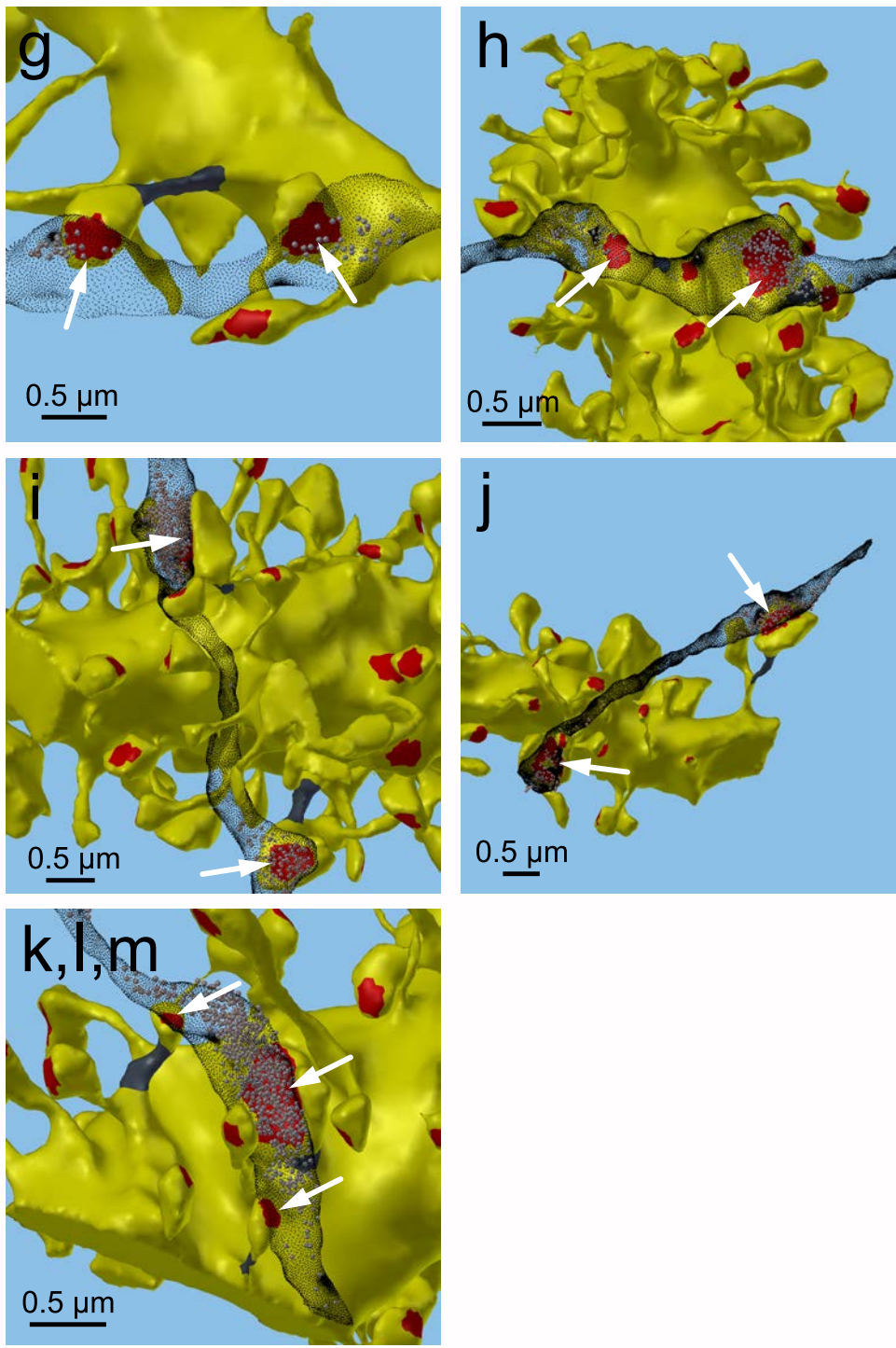


Figure S5

Fig. S5. Axon-coupled same-dendrite pairs g-m, illustrated in same way as in Fig. S4.

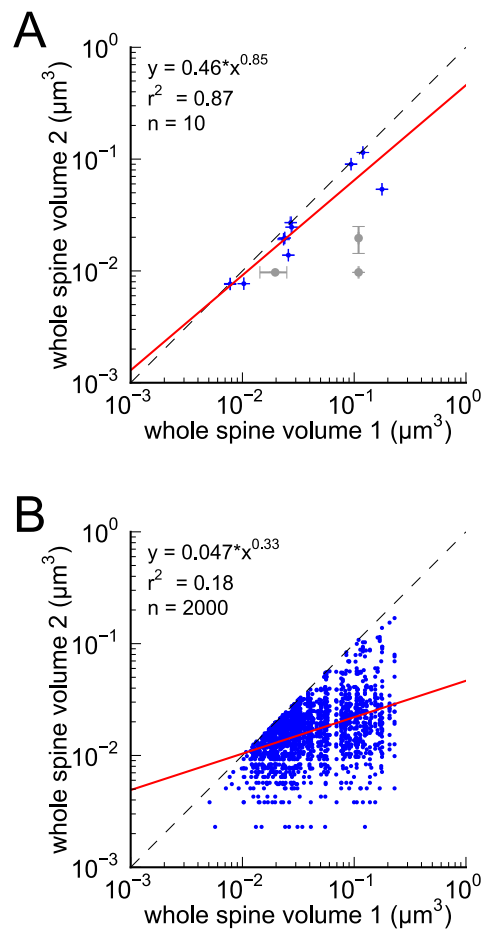


Figure S6

Fig. S6. Analysis of whole spine volumes of pairs of axon-coupled same dendrite spines. A) Whole spine volumes of pairs of axon-coupled spines on the same dendrite are highly correlated and significantly different (KS, $p = 0.018$) from B) whole spine volumes of random pairs.

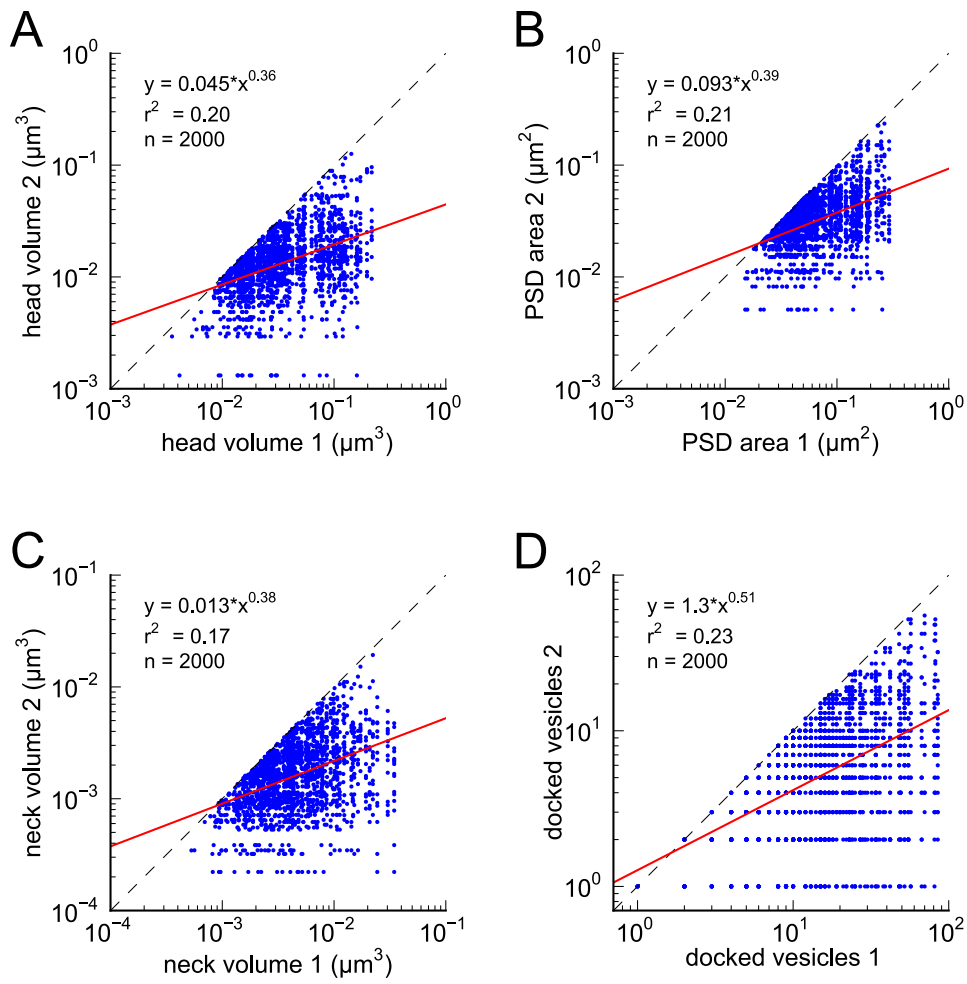


Figure S7

Fig. S7. Analysis of spines paired randomly. Distributions represent random pairings of A) spine head volumes, B) PSD areas, C) neck volumes, and D) docked vesicles, from the population of complete spines in the reconstruction. Larger value in each pair is plotted on the X axis. Regression lines shown in red. Error bars for each data point are not shown for clarity. Equations are based on regression of log-log distributions, with r^2 values indicated.

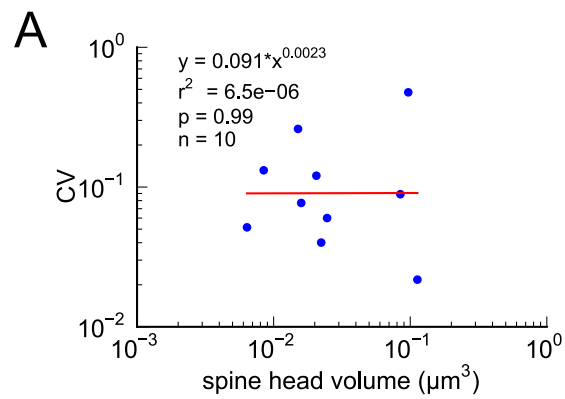


Figure S8

Fig. S8. CV of axon-coupled spines on the same dendrite does not vary with spine size.
There is no significant correlation, which implies that paired small synapses are as precisely matched as paired large synapses.

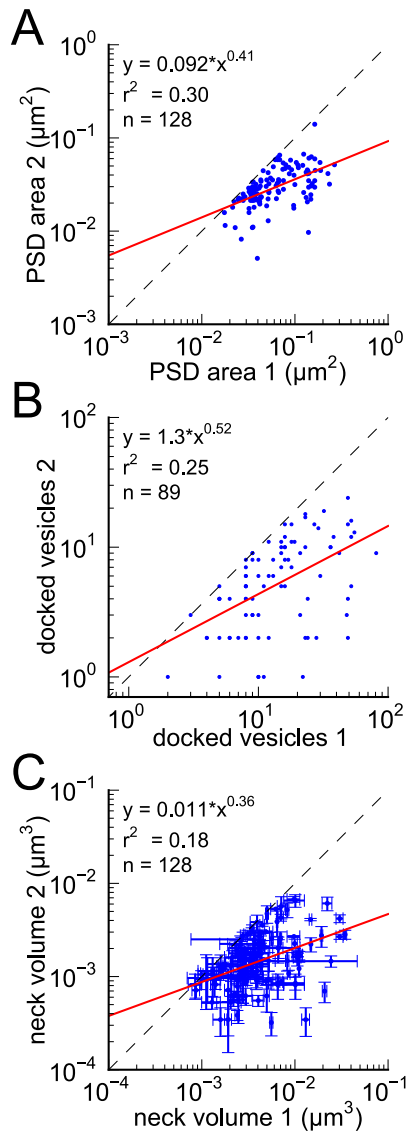


Figure S9

Fig. S9. Morphologies of PSD, docked vesicles, and necks are not correlated when spines are not both axon and dendrite coupled. There is no correlation between A) PSD area, B) docked vesicles, and C) neck volumes in pairs of axon-coupled spines on different dendrites.

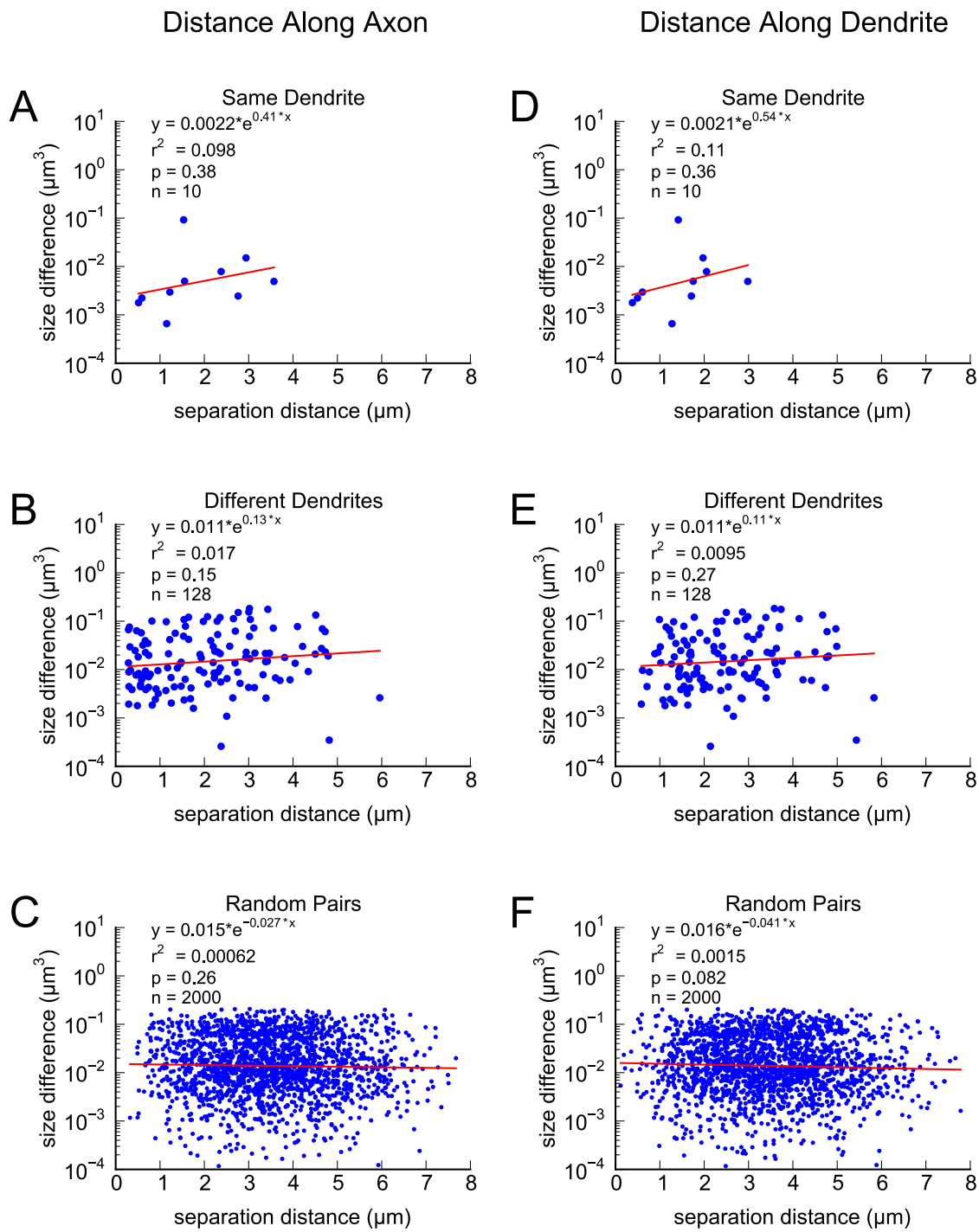


Figure S10

Fig. S10. Difference in volume between pairs of spines is not correlated with separation distance. A) Distance along the axon for axon-coupled spines on the same dendrite. B) Distance along the axon for axon-coupled spines on different dendrites. C) Distance along the axon for randomly paired spines. D) Distance along the dendritic branch for axon-coupled spines on the same dendrite. E) Distance along the dendritic branch for axon-coupled spines on different dendrites. F) Distance along the dendritic branch for randomly paired spines.

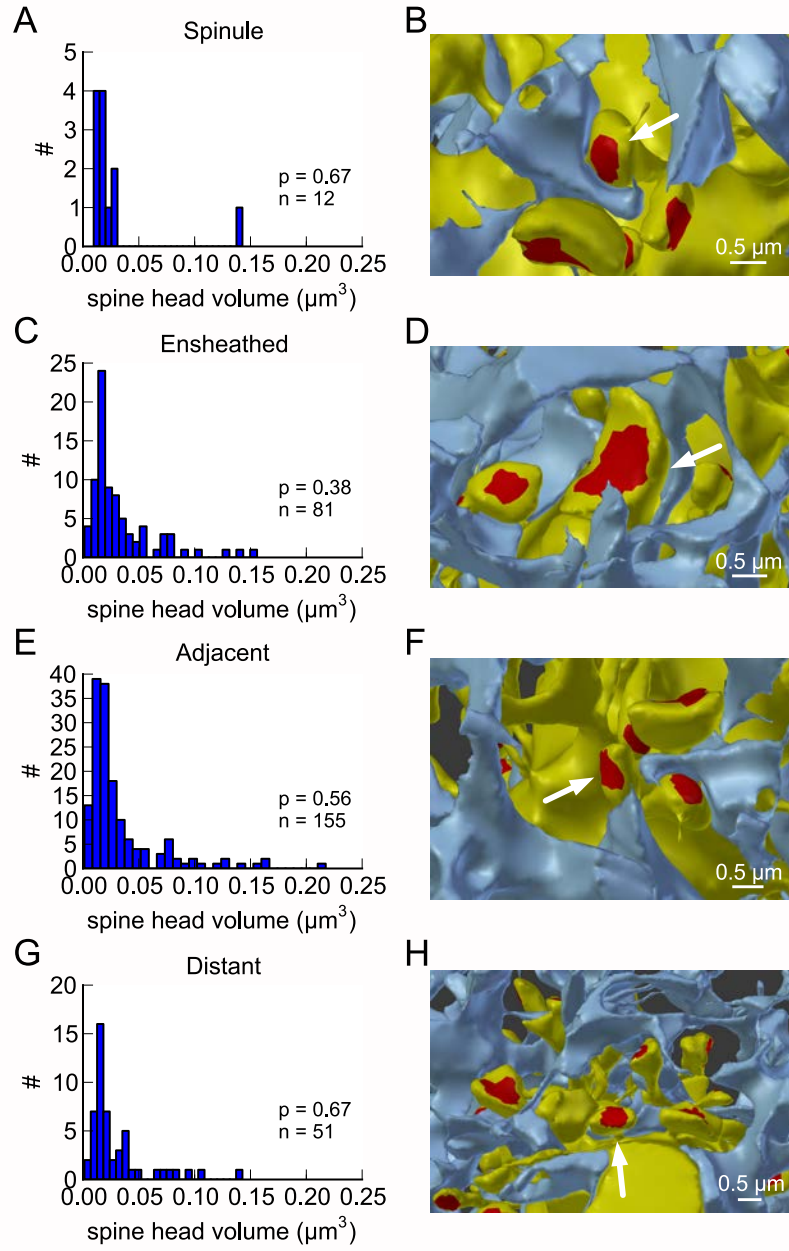


Figure S11

Fig. S11. Proximity of the glial cell to axon-coupled dendritic spines on either the same or different dendrites. Proximity of astrocytic glial processes is not significantly correlated with spine head volumes of axon coupled pairs. A) Histogram of spine head volume for spines that contain a spinule that is engulfed within the glial process (“spinule”). B) Representation of an engulfed spinule. C) Histogram of spine head volume for spines that are surrounded by and making contact with a glial process (“ensheathed”). D) Representation of “ensheathed” spine. E) Histogram of spine head volume for spines that are proximal but not contacting a glial process (“adjacent”). F) Representation of “adjacent” spine. G) Histogram of spine head volume for spines that are distant from any glial process. H) Representation of a spine “distant” from the glial process. The KS p value is shown on each inset and indicates that none of these distributions differ from the distribution for the whole population of spines.

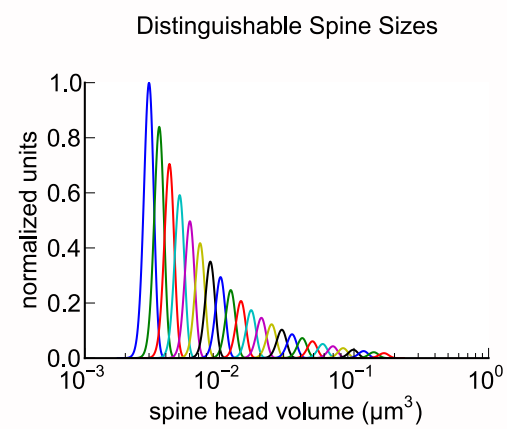


Figure S12

Fig. S12. Distinguishable spine sizes. Over the factor of 60 range in spine head volumes from the dataset there are 24 distinguishable intervals of spine sizes with a discrimination probability of 75% for each interval. The graph illustrates how distinct Gaussian distributions of spine sizes, each with a certain mean size and standard deviation, covers the entire range of spine head sizes. The CV of each distribution is a constant value of 0.083 (Fig. S8) and the intervals are spaced to achieve a total of 25% overlap with adjacent intervals giving a 75% discrimination threshold (see Methods). Note that the constant CV observed in the dataset (Fig. S8) means that the intervals appear uniformly spaced on a logarithmic scale. This is a form of non-uniform quantization which efficiently encodes the dynamic range of synaptic strengths at constant precision.